# Mixing of the Storfjorden overflow (Svalbard Archipelago) inferred from density overturns

Ilker Fer

Geophysical Institute, University of Bergen, Bergen, Norway

Ragnheid Skogseth

University Centre in Svalbard, Longyearbyen, Norway

Peter M. Haugan

Geophysical Institute, University of Bergen, Bergen, Norway

Bjerknes Centre for Climate Research, Bergen, Norway

[1]   Observations were made of the dense overflow from Storfjorden from a survey conducted at closely spaced stations in August 2002. The field data set consists of conventional conductivity-temperature-depth profiles and short-term moored current meters and thermistor strings. Finestructure estimates were made by calculating Thorpe scales over identified overturns using 0.1-dbar vertically averaged density profiles. Dissipation rate of turbulent kinetic energy per unit mass, $\varepsilon$, is estimated assuming proportionality between Thorpe and Ozmidov length scales. Vertical eddy diffusivity $K_z$ is estimated using Osborn's model assuming a constant mixing efficiency. Survey-averaged profiles suggest enhanced mixing near the bottom with values of $K_z$ and $\varepsilon$, when averaged within the overflow, equal to $10 \times 10^{-4}$ m$^2$ s$^{-1}$ and $3 \times 10^{-8}$ W kg$^{-1}$, respectively. $K_z$ is found to decrease with increasing buoyancy frequency as $N^{-1.2\ (\pm 0.3)}$, albeit values of N covered only $0.5-8$ cph (1 cph $= 2\pi/3600$ s$^{-1}$). Values of heat flux obtained using $K_z$ suggest that the plume gains a considerable amount of heat, $45 \pm 25$ W m$^{-2}$, when averaged over the thickness of the plume, from overlying waters of Atlantic origin. This value is lower than but, considering the errors in estimates of $K_z$, comparable with 100 W m$^{-2}$, the rate of change of heat in the overflow derived from sections across the sill and 80 km downstream.     INDEX TERMS: 4568 Oceanography: Physical: Turbulence, diffusion, and mixing processes; 4207 Oceanography: General: Arctic and Antarctic oceanography; 4219 Oceanography: General: Continental shelf processes; 4243 Oceanography: General: Marginal and semienclosed seas; KEYWORDS: mixing, Storfjorden overflow, Thorpe scale

## 1.   Introduction

[2]   The broad continental shelves of the Arctic Ocean, in winter, are sites of active water mass transformations, particularly in their coastal polynyas. Polynyas are ice-free areas, in a typically ice-covered region, due to climatologic conditions, formed and maintained by advection of ice by offshore winds and currents (latent heat polynyas) or melting due to upwelling warm water (sensible heat polynyas). They are distinguishable by their persistence and long durations from the short-lived leads [see, e.g., Wadhams, 2000]. When a latent heat polynya opens, intense heat loss to the atmosphere can lead to rapid and persistent ice formation, unlike sensible heat polynyas which require more intensive heat loss due to upwelled warm water.

Subsequent brine rejection and shelf convection form dense, brine-enriched shelf waters (BSW) that help to maintain the cold upper halocline of the Arctic Ocean [Aagaard et al., 1981]. Deep and bottom waters of the world ocean are partly formed through shelf convection [for a review see Killworth, 1983]. According to Rudels and Quadfasel [1991], shelf convection contributes about 0.5 Sv (Sv $\equiv$ $10^6$ m$^3$ s$^{-1}$) to the Arctic deep water. Cavalieri and Martin [1994] estimate $0.7-1.2$ Sv of BSW produced by the entire Arctic coastal polynyas, comparable to open ocean convection in the Greenland Sea [Smethie et al., 1986]. The BSW produced in basins of the Arctic continental shelves accumulates near the bottom and eventually spills toward the deep sea. Upon reaching the shelf edge, the dense plume descends the continental slope following a path governed by the combined effects of pressure gradient, frictional forces and the Coriolis force [Griffiths, 1986; Price and Baringer, 1994]. During its descent, the dense layer entrains and
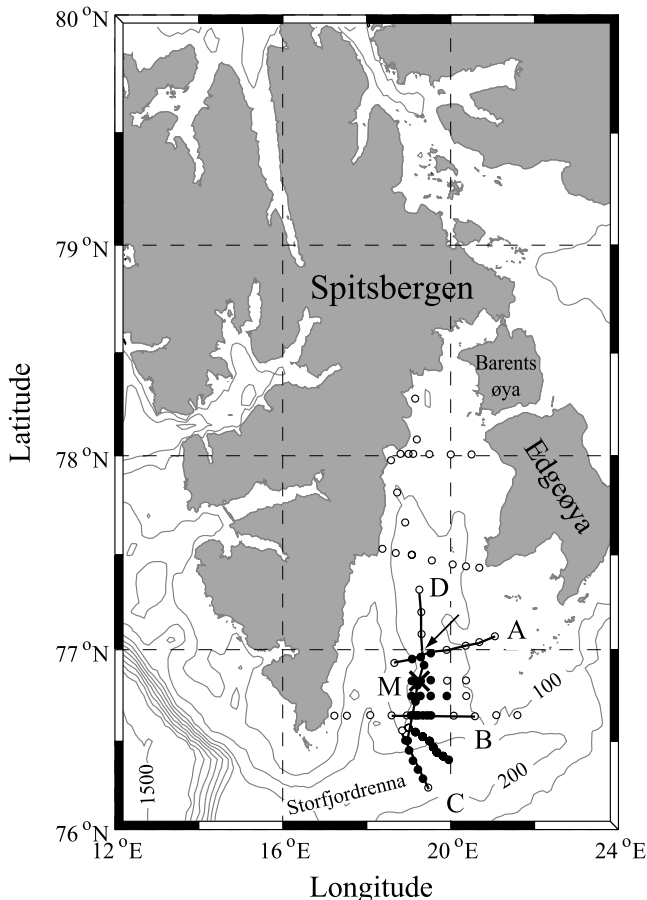
**Figure 1.** Map and bathymetry of the region. Isobaths are drawn at 100-m intervals until 1000 m. The 1500-m isobath is added. Circles show the location of the CTD stations. Those identified by dots denote the stations where plume was detected. Mooring M position is marked by a cross. Arrow points the approximate location of a 120-m deep sill. Sections A (Figure 7), B (Figure 8), C (Figure 9), and D (Figure 3) are also shown by lines joining corresponding stations.

mixes with ambient water. Such high-latitude overflows are bottom-intensified density currents with energetic and dissipative behavior and are a major element of the large-scale thermohaline circulation. They are, in general, poorly represented in ocean circulation models because of their associated small spatial scales, which can be improved by detailed process studies.

[3] Observations in Storfjorden in the southeastern Svalbard Archipelago (Figure 1) reveal that significant quantities of dense water originate through ice formation due to large heat loss in its polynya, particularly during northeasterly winds [see, e.g., *Haarpaintner et al.*, 2001]. The accumulated dense BSW, after reaching a 120-m deep sill, descends like a bottom gravity current following the topography spreading south through Storfjordrenna, a depression extending from Storfjorden area to the shelf edge (Figure 1), toward the shelf break and northward along the eastern side of Fram Strait [*Anderson et al.*, 1988; *Quadfasel et al.*, 1988]. This path is supported by the numerical model

results of *Jungclaus et al.* [1995] who applied a hydrostatic, transient reduced gravity plume model that allows for entrainment. Their results also suggest another branch of the plume that flows southward, guided by the topography, into a deep trench. Storfjorden is estimated to supply about 5–10% of the newly formed waters of the Arctic Ocean [*Quadfasel et al.*, 1988]. *Schauer* [1995] used hydrographic data and moored current meters sampling over a 1-year period in 1991/1992 to estimate a transport of 0.13 Sv of BSW during 5 months of strong and persistent overflow and 0.05 Sv when averaged annually. Recently, *Fer et al.* [2003] investigated the mixing and spreading of the overflow during May 2001 using velocity and conductivity- temperature-depth (CTD) profiles in the outer part of Storfjordrenna. The net volume transport out of a section close to the sill was estimated to be 0.06 Sv, which nearly doubled by the furthest downstream section. The model results yield a transport of 0.11 Sv [*Jungclaus et al.*, 1995], comparable to the field observations. Using results from long-term time series observations of currents, hydrography and a benthic tripod, *Sternberg et al.* [2001] reported that the overflow during fall and winter can resuspend sediments.

[4] Here we present observations of mixing of the Storfjorden overflow from a survey conducted at closely spaced stations in August 2002. The ice formation and BSW production in the basin (R. Skogseth and P. M. Haugan, Ice and brine production in Storfjorden from four winters of satellite and in situ observations, submitted to the *Journal of Geophysical Research*, 2003) and its hydrography (R. Skogseth et al., Water mass transformations in Storfjorden, submitted to the *Continental Shelf Research*, 2003) are topics for other works and are not discussed in this paper. The field data set consists of conventional CTD profiles and short-term moored instruments. The site, details of the survey and large-scale observations are described in section 2. Subsequently, estimates of mixing parameters are summarized in section 3 followed by a discussion of the results (section 4). Throughout this paper potential temperature, θ, is used. Salinity, S, is given on the practical salinity scale, and $\sigma_\theta + 1000$ is the potential density in kg m$^{-3}$, referenced to surface.

## 2. Site and Large-Scale Observations

[5] Storfjorden located in the southeastern Svalbard Archipelago is approximately 190-km long and 190-m deep at its maximum depth and is enclosed by Spitsbergen, Barentsøya, and Edgeøya and limited by a shallow bank, Storfjordbanken, in the southeast and a 120-m deep sill (identified by an arrow in Figure 1) at about 77°N in the south. Its bathymetry is shown in Figure 1. The basin, north of the sill, covers an area of about $13 \times 10^3$ km$^2$ with an approximate volume of $8.5 \times 10^{11}$ m$^3$.

[6] Observations were made of the overflow of the BSW plume from Storfjorden at densely spaced hydrographic stations occupied by R/V *Håkon Mosby* during 3–15 August 2002. CTD measurements were made at stations shown in Figure 1 using a SBE911*plus* which was lowered at a rate of about 0.7 m s$^{-1}$ as close as 1 m to the bottom. The sensor accuracies of the CTD instrument are provided by the manufacturer as 1 dbar, $1 \times 10^{-3}$°C, and $3 \times 10^{-4}$ Siemens m$^{-1}$ for pressure, temperature and conductivity, respectively. A mooring (M, for location see Figure 1)
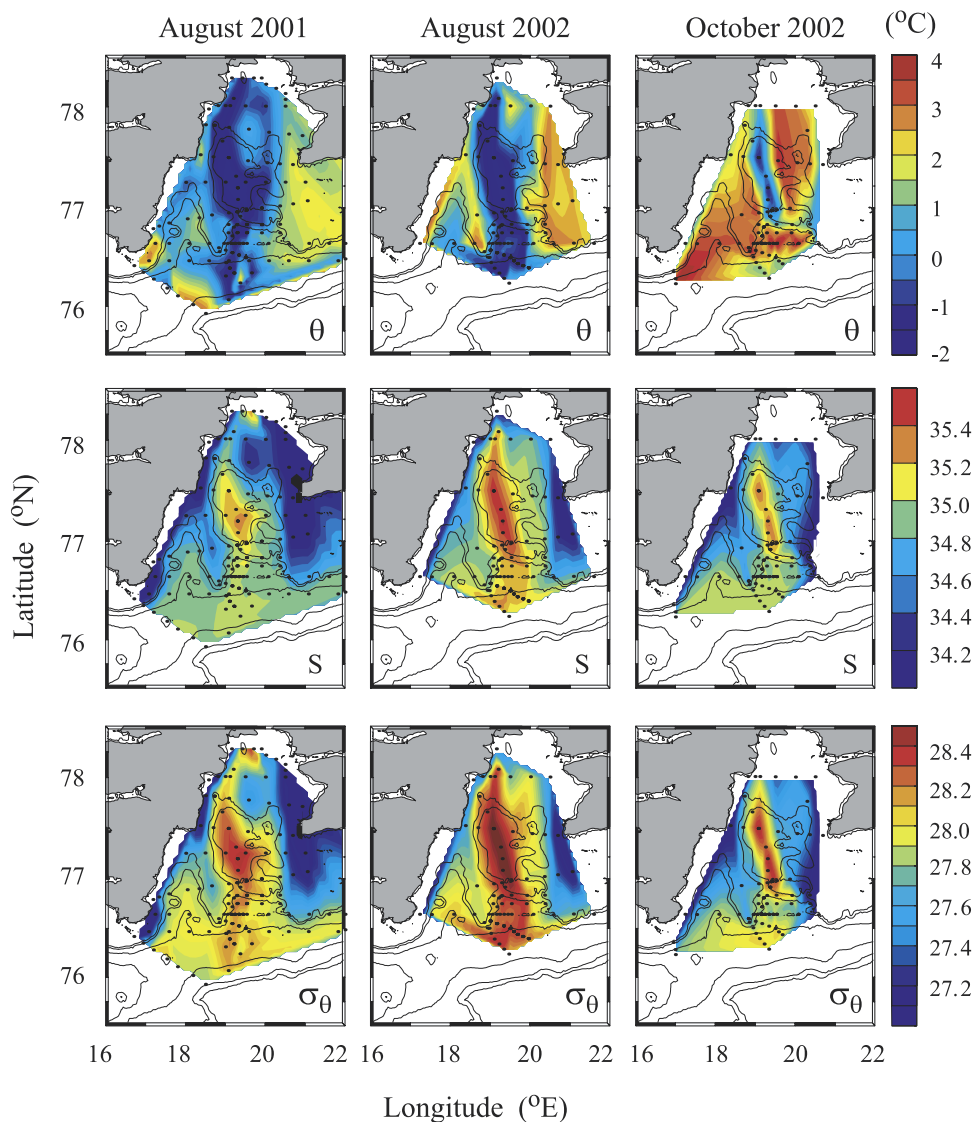
**Figure 2.** Distribution of potential temperature θ, salinity S, and σ_θ derived from bottom values measured in August 2001 and 2002 and October 2002 at stations indicated by dots.

consisting of a water level recorder at 2-m height above bottom (hab), two RCM7 Aanderaa current meters at 3 and 7-m hab, and a 50-m thermistor string with 11 sensors of 5-m vertical separation, covering 10–60-m hab, was deployed at 76°49.8′N, 19°15.5′E over 132-m isobath, approximately 16 km downstream of the sill (Figure 2). Data were recorded for 104 h starting from 7 August 2002, 1600 UTC, every 5 min for the thermistor string and 10 min for the other instruments. Both current meters were equipped with temperature and pressure sensors and that at 3-m hab also had a conductivity sensor. Salinity and temperature data recorded by the moored instruments were calibrated against those of the CTD casts made prior to and after the deployment and recovery of the moorings.

[7] The overflow of dense BSW shows interannual variability and its path and strength depends mainly on the initial salinity in the basin, the dynamics of the polynya and resulting rate of ice formation. Variability of the surface salinity in the western Barents Sea associated with the ice

transport from the Arctic Ocean [*Maus*, 2002] and large-scale atmospheric circulation in the North Atlantic are thought to have effects on this variability. A comparison of bottom temperature, salinity and density between those derived from surveys carried out in August 2001 and 2002 (Figure 2) shows that the bottom water in the basin had higher salinity and hence density in 2002, leading to a strong overflow. Observations of the overflow in 2002, reported here, can be regarded as exceptional because CTD profiles taken from R/V *Oden* in April show the highest ever recorded bottom salinity reaching 35.8 in the vicinity of the deepest pool of Storfjorden (B. Rudels, personal communication). Furthermore, the month following our survey, in September 2002, *Schauer et al.* [2003] observed a plume of high density in the deep Fram Strait, at 1950-m water depth at West Spitsbergen continental slope at 78°50′N, where no indication of dense shelf water was found in the preceding five years, between 1997–2001. Here, the plume was about 60-m thick associated with
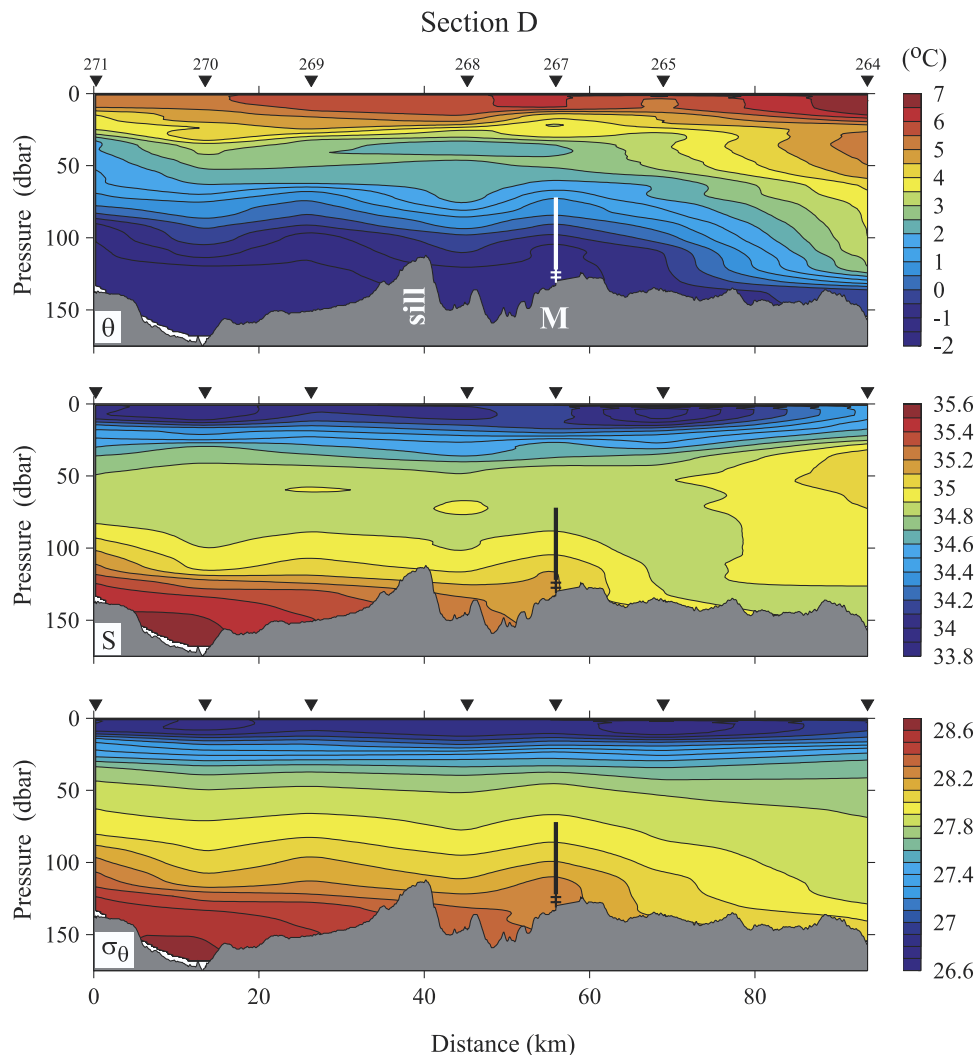
**Figure 3.** Contours of potential temperature θ, salinity S, and $\sigma_\theta$ derived for section D (Figure 1) using profiles taken at the stations indicated by arrowheads over each panel. Profiles are 1-dbar-averaged and smoothed over 6 data points. Contour intervals are 0.5°C for θ, 0.1 for S, and 0.1 kg m$^{-3}$ for $\sigma_\theta$, respectively. The section was worked on 7 August 2002, and the duration of measurements to complete the section was 7.5 hours. The position of the mooring, consisting of a water level recorder at 2-m hab, two RCM7s at 3- and 7-m hab, and a thermistor chain covering 10–60-m hab, is also shown.

anomalies in salinity and temperature of 0.03 and 0.25°C, respectively. Approximately one month later, in October, the dense water at the bottom was trapped behind the sill after the overflow has ceased prior to the survey (Figure 2). The previous incident when Storfjorden overflow could be traced down into the Fram Strait was in August 1986 [*Quadfasel et al.*, 1988] and the corresponding maximum salinity in the basin was 35.4. This is 0.1 units less than that observed in August 2002 (Figure 2), hence the ice production and maximum salinity in April 1986 could be comparable to that in 2002. In August 2000, a survey worked by R/V *Håkon Mosby* showed S = 35.45 at the deepest part of Storfjorden, and deep reaching overflow to the Fram Strait might be expected when compared with 1986 and 2002. However, no evidence of Storfjorden plume was observed west of Spitsbergen in 2000 by *Schauer et al.* [2003], probably because of difficulties in detecting the plume because of small spatial scale and intermittent occurrence.

[8] Contours of θ, S, and $\sigma_\theta$ derived from the measurements conducted in August 2002 along the longitudinal section D are shown in Figure 3. The most saline, densest water is seen in the basin, behind the sill. The surface cap is warm and fresh because of summer heating and melting. The plume reaches the farthest downstream station. It should be noted that this section follows the onshore edge of the plume rather than its core (see Figures 7–9 on which the approximate location where section D crosses sections A–C are shown by arrows marked by D) and therefore does not represent the highest density of the overflow. Core stations are not aligned to derive a section, because large time differences between each station would lead to deviations from the synoptic picture due to possible tidal influences and lateral variations. Atlantic Water (AW) is recognized between stations 264 and 265 with S ∼ 35 and θ in excess of 3°C.
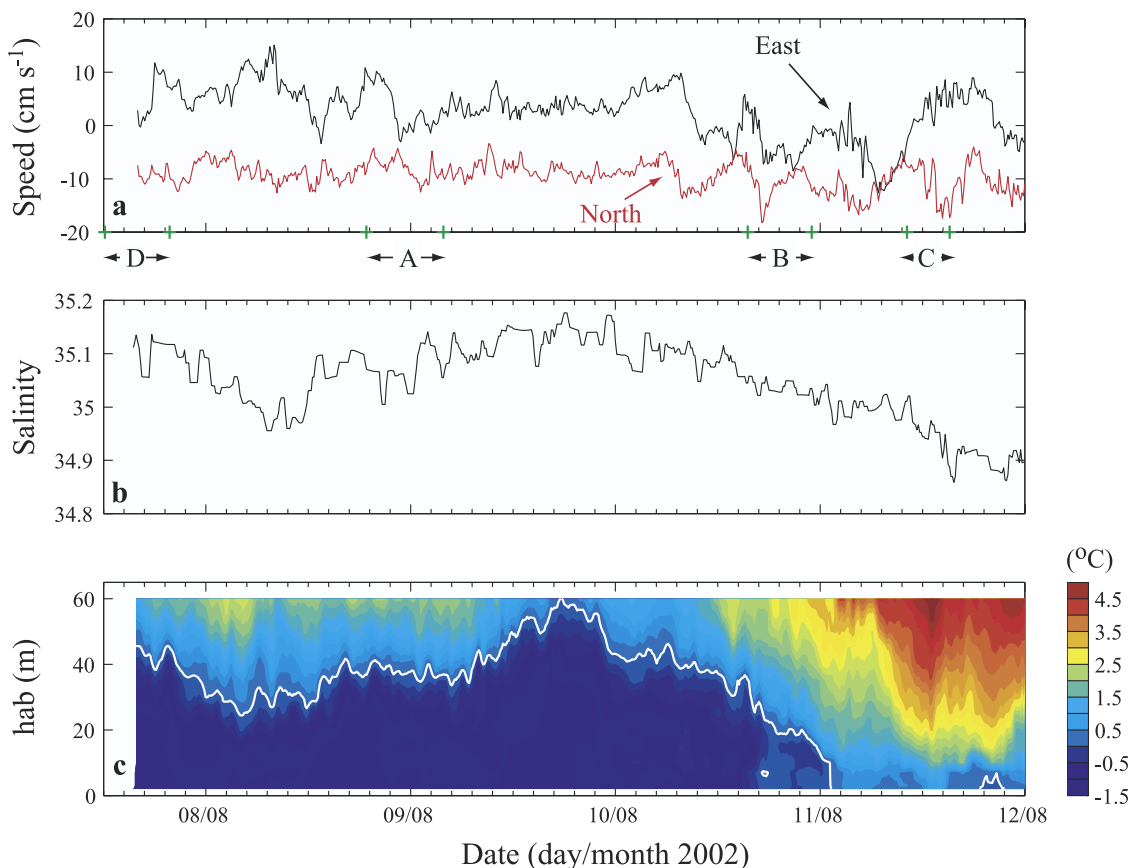
**Figure 4.** Detided time series of (a) east (black) and north (red) components of velocity recorded at 7-m hab, (b) salinity at 3-m hab, and (c) isotherms. Isotherms are derived from the temperature recorded by the thermistor chain, two Aanderaa current meters and a water level recorder. White isotherm is 0°C. Duration of sections A–D are also shown in Figure 4a.

[9] Time series recorded by the moored instruments are detided using tidal harmonic analysis [*Pawlowicz et al.*, 2002] and are illustrated in Figure 4. The data show the presence of a cold, close to the freezing point, and saline (S > 35) plume associated with downslope flow for the first three days of the record. When defined as water with $\theta <$ 0°C, the height of the plume at the mooring location varies between 20 and 60 m and equal to 40 ± 8 m, on the mean (± one standard deviation). After 84 h, AW with $\theta$ in excess of 4.5°C penetrates across the mooring. Its signature is observed as close as 3-m hab as can be seen from the salinity record with values of S gradually decreasing to 34.9 (Figure 4b) and the temperature record with $\theta >$ 0°C (Figure 5). Assuming that this is the tongue of AW seen in Figure 3, observed at the start of the recording period (see the time of occupation of section D in Figure 4a), it covers approximately 25 km giving a propagation speed of 8 cm s$^{-1}$ toward the sill. In Storfjordrenna, AW circulates in a cyclonic sense following the topography [*Schauer*, 1995; *Fer et al.*, 2003] as can be seen from the data recorded by the current meter at 3-m hab with westward velocity when $\theta >$ 0°C (Figure 5).

[10] The mean velocity derived over the duration of the plume is 10 cm s$^{-1}$ at 7-m hab directed 159° from true north. Corresponding values derived from the data recorded by the bottommost current meter at 3-m hab are 8 cm s$^{-1}$

and 152°. A progressive vector diagram produced from the along and cross-stream components at 3-m hab suggests that water with $\theta <$ 0°C reaches ∼25 km downstream of the mooring position (Figure 5). Streamwise coordinates are obtained after rotating the velocity 28° counterclockwise from north. Using the average thickness, h = 40 m, and speed, u = 0.1 m s$^{-1}$ observed from the thermistor string and the current meter at 7-m hab, respectively, an estimate for transport equal to 0.12 (±0.04) Sv can be obtained provided that the cross section is rectangular with an approximate width of 30 km (see Figures 7c and 8c). The uncertainty here is derived from the variability in height and the uncertainty in width of the plume. Higher uncertainty will arise if the section-averaged downstream velocity is significantly different than 0.1 m s$^{-1}$. The volume transport compares well with those reported in the literature (section 1).

## 3. Estimation of Turbulence Quantities From Density Overturns

### 3.1. Methods

[11] In a stratified fluid, a parcel of fluid has to move a vertical distance which as a statistical mean can be represented by the Ozmidov scale, $L_O = (\varepsilon/N^3)^{1/2}$, in order to convert all its kinetic energy into potential energy [*Ozmidov*,
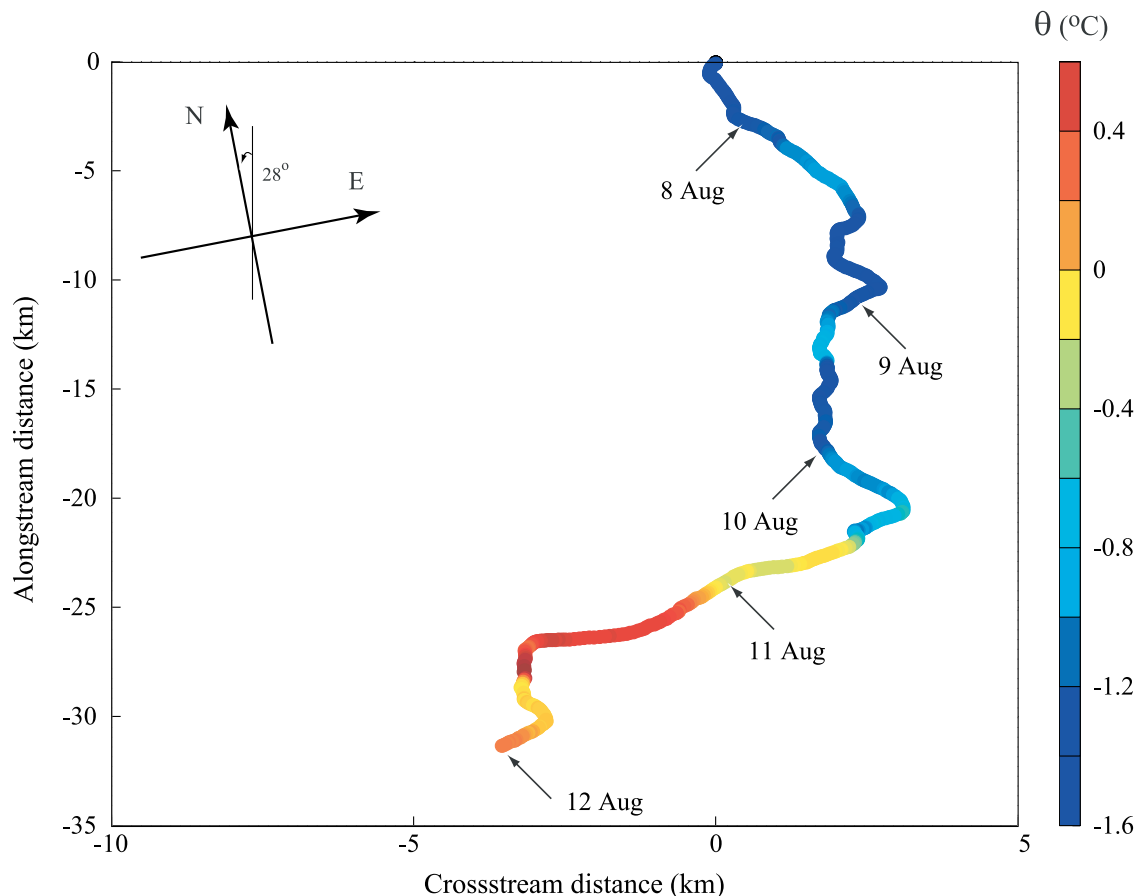
**Figure 5.** Temperature-coded (color) progressive vector diagram derived from the along- and cross-stream components of velocity recorded at 3-m hab. Date given at 0000 UTC are indicated by arrows.

1965]. Here, $\varepsilon$ is the dissipation of turbulent kinetic energy per unit mass and $N$ is the buoyancy frequency. Using conventional CTD profiles, *Thorpe* [1977] developed a method to estimate the length scales of overturns associated with gravitational instabilities in a stratified turbulent flow. Working in fresh water, he used temperature profiles representative of density which he reordered into a gravitationally stable profile, i.e., temperature ($>4°C$) decreasing with increasing depth. The Thorpe scale, $L_T$, can then be calculated as the root mean square (rms) value of all nonzero displacements that each parcel of fluid has to move vertically from the initial to the reordered profile within the depth span covering the overturn. He suggested that $L_T$ should be proportional to $L_O$, a relation later investigated and confirmed by *Dillon* [1982] who used oceanic temperature microstructure data to find that $c = L_O/L_T \approx 0.8$ in the seasonal thermocline and deep in the interior of wind-forced surface mixed layers. More recently, *Ferron et al.* [1998] obtained $c = 0.95$ ($\pm 0.6$) in the Romanche Fracture zone using temperature microstructure data for $\theta < 2°C$.

[12] It is generally preferred to assume that density overturns can be represented by the overturns in potential temperature to eliminate relatively high instrumental noise in the conductivity cell as well as the systematic noise due to mismatches in time response of temperature and conductivity probes or the thermal inertia of the conductivity cells.

However, to avoid spurious inversions, density should be used when salinity is the stratifying agent or different water masses are present. *Galbraith and Kelley* [1996] propose a scheme in which they eliminate overturns due to random noise and systematic noise by "run length" and "water mass" tests, respectively. The latter requires tight relationships between density, temperature and salinity within overturns. Normalized deviations between observations and best line fits to density-S and density-$\theta$ scatters yield ratios that exceed unity for loose relationships. The "run length" test yields a threshold for the density noise, after comparing the probability density function of the run length with that of random noise, which is typically greater than that derived from resolutions of temperature and conductivity sensors provided by the manufacturers.

[13] Finestructure estimates were made by calculating $L_T$ over overturns identified by the scheme proposed by *Galbraith and Kelley* [1996] using downcast data from 0.1-dbar vertically averaged density profiles. Buoyancy frequency, $N$, is calculated over each identified overturn from the reordered, gravitationally stable density profiles. Then assuming $L_O = cL_T$, an estimate for $\varepsilon = (cL_T)^2 N^3$ is obtained using the definition of $L_O$ with $c = 0.8$. Vertical eddy diffusivity is estimated on the basis of the turbulent mass flux, using *Osborn*'s [1980] model as $K_z = \gamma \varepsilon/N^2$ where the mixing efficiency, $\gamma = R_f/(1 - R_f)$, is a function
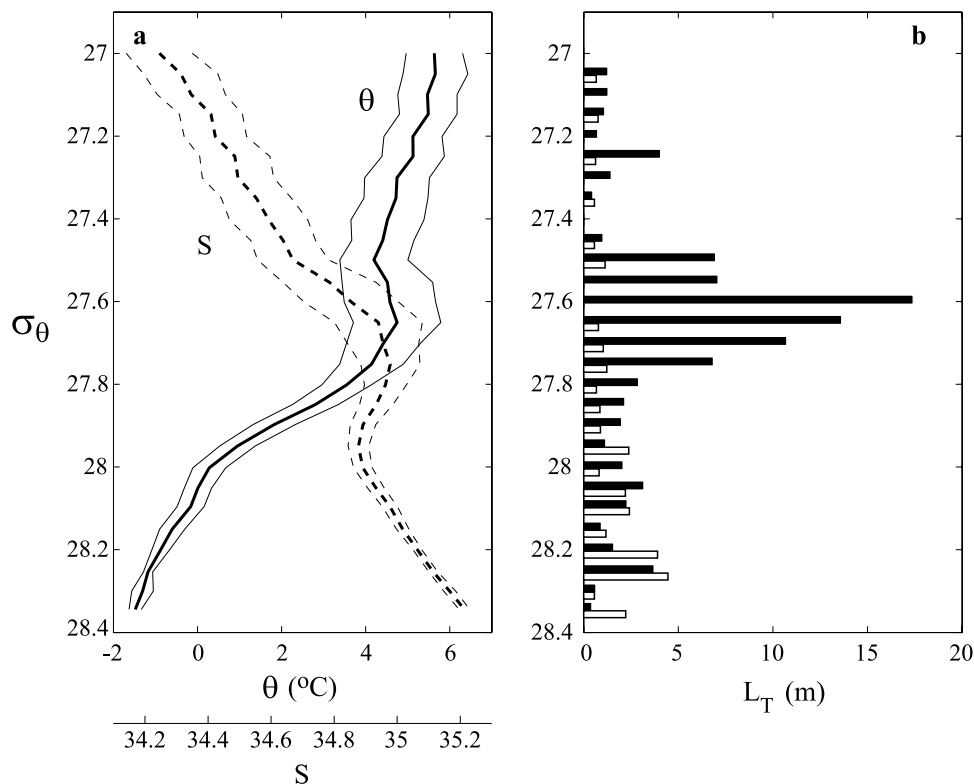
**Figure 6.** (a) Mean potential temperature θ (solid line) and salinity S (dashed line) profiles as a function of $\sigma_\theta$. Envelopes denote one standard deviation. (b) Comparison of the Thorpe scales derived using only temperature (solid bars) and density (open bars) profiles. Note that the temperature-derived Thorpe scales are unrealistic because of the presence of warm water at $27.5 < \sigma_\theta < 27.8$ that leads to unstable overlying water but is compensated by salinity in density profiles. Therefore we use density profiles in our mixing estimates.

of the flux Richardson number, $R_f$. Osborn's model assumes steady, homogeneous turbulence field where the production of turbulent kinetic energy by the Reynolds stress working against the mean shear is balanced by ε and the production of buoyancy. Mixing efficiency indicates the conversion efficiency of turbulent kinetic energy into potential energy of the system. It is commonly taken to be 0.2 [*Gregg*, 1987], however can vary depending on the dynamics generating turbulence (section 3.2). We use γ = 0.15 in our calculations. The uncertainties associated with the estimates are discussed in the following section.

[14] The standard sampling rate of the CTD is 24 Hz and with the nominal descent rate of 0.7 m s$^{-1}$, this corresponds to a sampling greater than 3 data per 0.1 dbar. When calculated over all profiles, 91% of the bins comprise ≥2 data points. In order to avoid nonmonotonic pressure series as a result of ship roll in the surface wave field, pressure data are low-pass filtered with a time constant of 0.15 s and scans were flagged and excluded from bin averaging when CTD descent rate was less than 0.25 m s$^{-1}$. On the basis of combined statistics of all profiles, a cutoff run length of 6 was chosen below which overturns are assumed to be created by noise. The noise level in density measurements based on this run length is 0.0016 kg m$^{-3}$. The threshold for water mass test was set to 0.75. This is larger than the threshold of 0.5 suggested by *Galbraith and Kelley* [1996] which was obtained by visual inspections of loops in

θ-S diagrams. This threshold was relaxed in this study since no prominent loops were observed. Furthermore, in our case where θ is close to the freezing point, the variation in density with temperature alone is not significant.

[15] The necessity of using profiles of density as discussed above is demonstrated in Figure 6. Using 33 casts from the stations where the plume was detected, mean θ and S profiles are calculated as a function of $\sigma_\theta$ (Figure 6a). The mean values are obtained by taking the average of all θ and S falling into bins of 0.05 $\sigma_\theta$ unit increments. Thorpe scales, separately derived from profiles of density and θ, are averaged in a similar fashion and contrasted in Figure 6b. In detection of overturns from θ-depth profiles a noise threshold of $5 \times 10^{-3}$°C is used. The agreement between the two estimates is poor, particularly in the 27.5–27.8 $\sigma_\theta$ class, where overlying water is relatively colder, hence unstable with respect to temperature. Here, θ-derived $L_T$ values exceed 15 m, suggesting intense overturns, whereas those derived from density are within 1.5 m. On the average, when derived from θ, $L_T$ is 2.6 times larger.

## 3.2. Isotropy and Errors
### 3.2.1. Isotropy

[16] When turbulence is isotropic, the Reynolds-averaged turbulent kinetic energy equation gives $\varepsilon = 7.5 \, \nu \, \langle (du/dz)^2 \rangle$, where $\nu$ is the kinematic viscosity and du/dz is the vertical profile of the small-scale current shear and angle brackets

denote ensemble, or spatial as practically applied in oceanic microstructure studies, averaging [*Batchelor*, 1953]. In a stratified flow, the dimensionless ratio $\varepsilon/\nu N^2$, often referred to as buoyancy Reynolds number (or index for activity of turbulence), gives an indication of departures from small-scale isotropy, which is also assumed to be achieved in our estimates of turbulence quantities. When $\varepsilon/\nu N^2 > 20$, estimates approach to the isotropic formula [*Yamazaki and Osborn*, 1990] with error limited to less than 35% for lower values. This is also roughly the threshold below which mixing can no longer sustain the negative buoyancy flux necessary for a net increase in potential energy. The turbulence field can be considered isotropic for $\varepsilon/\nu N^2 \geq 200$ [*Gargett et al.*, 1984; *Yamazaki and Osborn*, 1990]. The average values of $\varepsilon$ and N within the plume are $3 \times 10^{-8}$ W kg$^{-1}$ and 2.5 cph (1 cph = $2\pi 3600^{-1}$ s$^{-1}$), respectively. Using $\nu = 1.8 \times 10^{-6}$ m$^2$ s$^{-1}$, this leads to a buoyancy Reynolds number of about 900, and we can use Osborn's model with confidence. Again using the average value of $\varepsilon$ in the plume, an estimate of $\langle (du/dz)^2 \rangle$ of O($10^{-3}$) s$^{-2}$ can be obtained for the small-scale shear. This is an order of magnitude greater than that of larger scale reported for the overflow in Storfjordrenna derived from profiles of current as well as geostrophy over 10-m vertical separations when the density excess of the plume was lower [*Fer et al.*, 2003].

### 3.2.2. Errors

[17] Dissipation rate of turbulent kinetic energy per unit mass is estimated from $\varepsilon = (cL_T)^2 N^3$, where c is the constant of proportionality between $L_O$ and $L_T$, here taken as c = 0.8. The above expression for $\varepsilon$ is sensitive to N, which is estimated from the reordered density profile over a depth range enclosing each particular overturn. Minor errors arise in N, associated with resolutions in density and depth. However, a comparison between values of N derived from the same vertical intervals as the overturn and those derived outside it, representative of the background N ($N_b$), manifests how much mixing the observed turbulent patch may have undergone at the time it was observed. We calculated $N_b$ including 0.5-m on either side of each overturn. The ratio of N to $N_b$ is approximately normally distributed covering a range 0.3–1 and equals to 0.65 ± 0.16 (± one standard deviation). The broad range suggests that the overturns, when observed, are at varying stages of their lifetimes. The variability in $\varepsilon$ over all events increases by a factor of 3 when derived using $N_b$. As discussed by *Dillon* [1982], fluctuation in the interior of an overturn can be quite insensitive to the stratification only a small distance away, provided that the mixing regime is different there. In order to be representative of the stratification against which the overturn is straining, N should be calculated over the depth range of the overturn. Another source of uncertainty in $\varepsilon$ is the choice of c. According to results of *Ferron et al.* [1998] given in section 3.1, the variability in c can be ~60%. A systematic error of 10% in finding $L_T$ together with the variability in c results in 140% error in $\varepsilon$. Furthermore, consideration of accuracy and assumption of isotropy may introduce additional errors, and $\varepsilon$ can be estimated to within a factor of 3.

[18] The diffusivity, $K_z = \gamma (cL_T)^2 N$ is less sensitive to N, but additional errors arise because of the mixing efficiency which is taken as $\gamma = 0.15$. The application of $N_b$ increases the variability in $K_z$ by a factor of 1.2. The uncertainty introduced by the choice of $\gamma$ is insignificant compared to that arising from the $L_O$ - $L_T$ relationship. As reported elsewhere [see *Peltier and Caulfield*, 2003], $\gamma$ may vary strongly depending on the type of instability and the different stages of turbulence transition, i.e., initial stage of instability amplification, development of secondary instabilities and three-dimensional collapse of turbulence. Neglecting values derived for tidal channel flows, typical values in the literature span a range of 0.15–0.3. As a result, $K_z$ can be estimated within a factor of 4. While this level of uncertainties in the present study may seem high, it should be noted that it is comparable to that of other turbulent studies in oceans or lakes. Furthermore, our conclusions on enhanced mixing within the overflow are drawn on the basis of variations that exceed one order of magnitude, well above the level of uncertainties.

## 4. Results and Discussion

### 4.1. Downstream Development

[19] The overflow is subject to mixing with overlying warmer waters of Atlantic origin and the extent to which the overflow water can retain its identity will depend on the intensity of mixing. Estimates of mixing parameters inferred from Thorpe-scale analysis for three representative sections across the overflow, looking in the upstream direction with Spitsbergen on the left, are presented in Figures 7–9, together with contours of $\theta$, S, and $\sigma_\theta$. In each figure, overturns are represented by boxes at the corresponding depth, with vertical length equal to the height of the overturn. Estimates of log($K_z$) and log($\varepsilon$) are color-coded in panels (a) and (b), respectively. The section at the sill (Figure 7) shows the weakest turbulent activity with a total of 8 distinguishable overturns, two of which are near the interface between the overflow and the ambient water. Thickness and extent of the plume is approximately shown by the isopycnal corresponding to $\sigma_\theta = 27.95$, consistent with *Fer et al.* [2003]. Farther downstream, at section B, the plume is well developed and is associated with enhanced $K_z$ and $\varepsilon$ with values one order of magnitude greater than those in the ambient. Turbulent patches associated with the overflow are more pronounced on the sloping side of the section where isopycnals are tilted, indicative of a geostrophically balanced overflow into Storfjordrenna. At section B, water of density exceeding 28.3 is no longer present compared to the transect at the sill where $\sigma_\theta$ reaches 28.6 immediately adjacent to the bottom. This is because of the intense mixing with the ambient water as the plume descends. The initial part of the overflow is particularly important since, until the rotational effects are well established within a Rossby radius of deformation (~4 km), the plume accomplishes most of its entrainment flowing downslope before it is slowed down by friction and deviated along the isobaths. Around the core of AW, which here can be identified by the S = 35 isohaline between 50–100-m depth, mixing may be due to frontal instabilities. As the plume propagates away from the sill toward the farthest downstream section (Figure 9), the vertical gradient of its density gradually decreases. This is consistent with the fact that encountered vertical mixing acts to homogenize the plume vertically. It is noteworthy that the last transect provides evidence for episodes of denser overflow encoun-
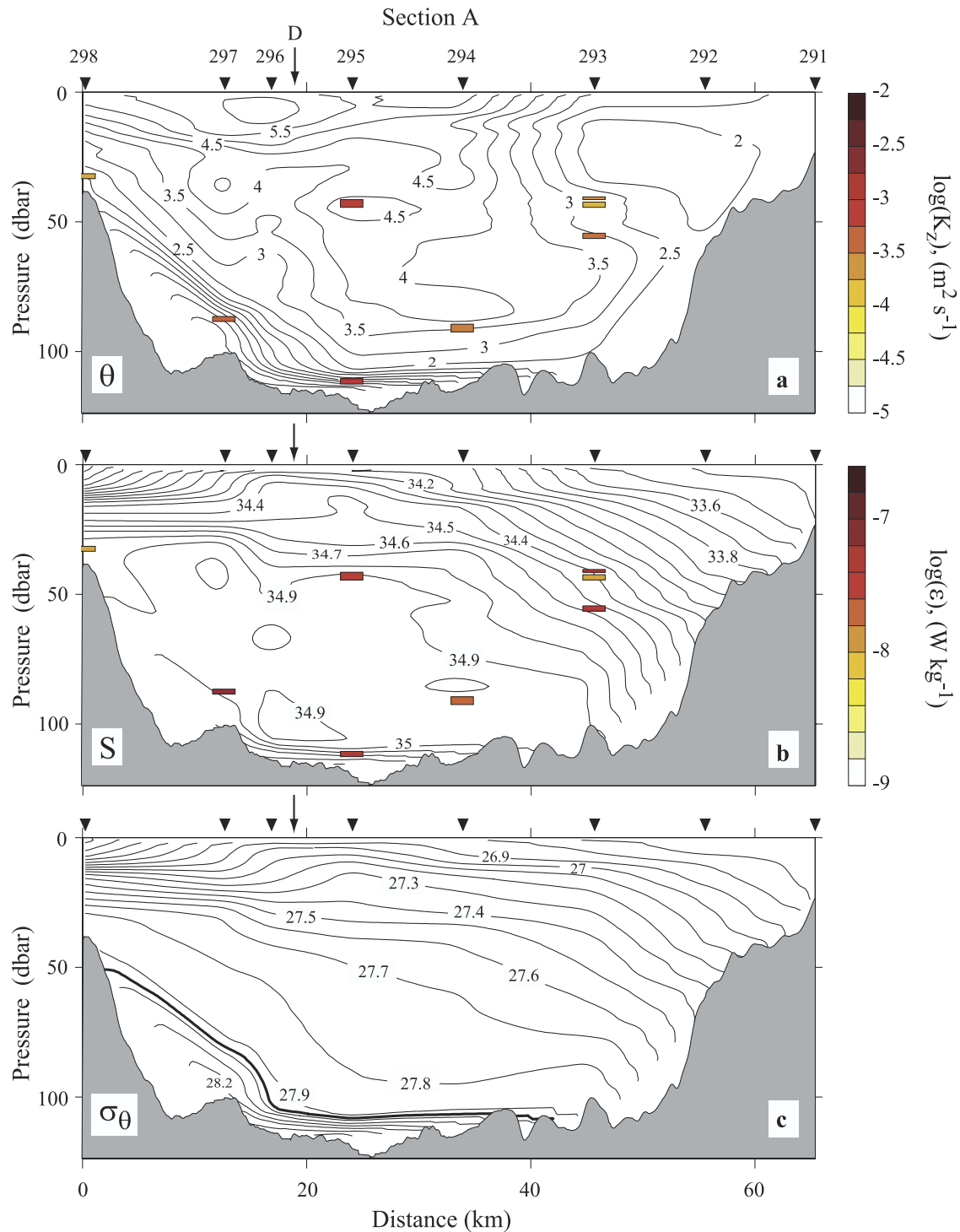
**Figure 7.** Distribution of (a) $\theta$ and vertical diffusivity $K_z$ (colored), (b) S and $\varepsilon$ (colored), and (c) $\sigma_\theta$ derived for section A (Figure 1). Each colored box in Figures 7a and 7b represents a detected overturn spanned by its height. The width of the boxes is arbitrary. The additional thick isopycnal in Figure 7c is $\sigma_\theta$ = 27.95 and roughly represents the extent of the plume [*Fer et al.*, 2003]. Profiles are taken at the stations numbered in Figure 7a and indicated by arrowheads over each panel. The arrow marked by D shows the approximate location where section D (Figure 3) crosses the section. The 1-dbar-averaged values are interpolated into a regular grid of 1-dbar bins in vertical and 150 distance bins in horizontal and smoothed over 6 data points. Contour intervals are 0.5°C for $\theta$, 0.1 for S, and 0.1 kg m$^{-3}$ for $\sigma_\theta$, respectively. Bottom topography is derived from echo sounding after correcting for the sound velocity.
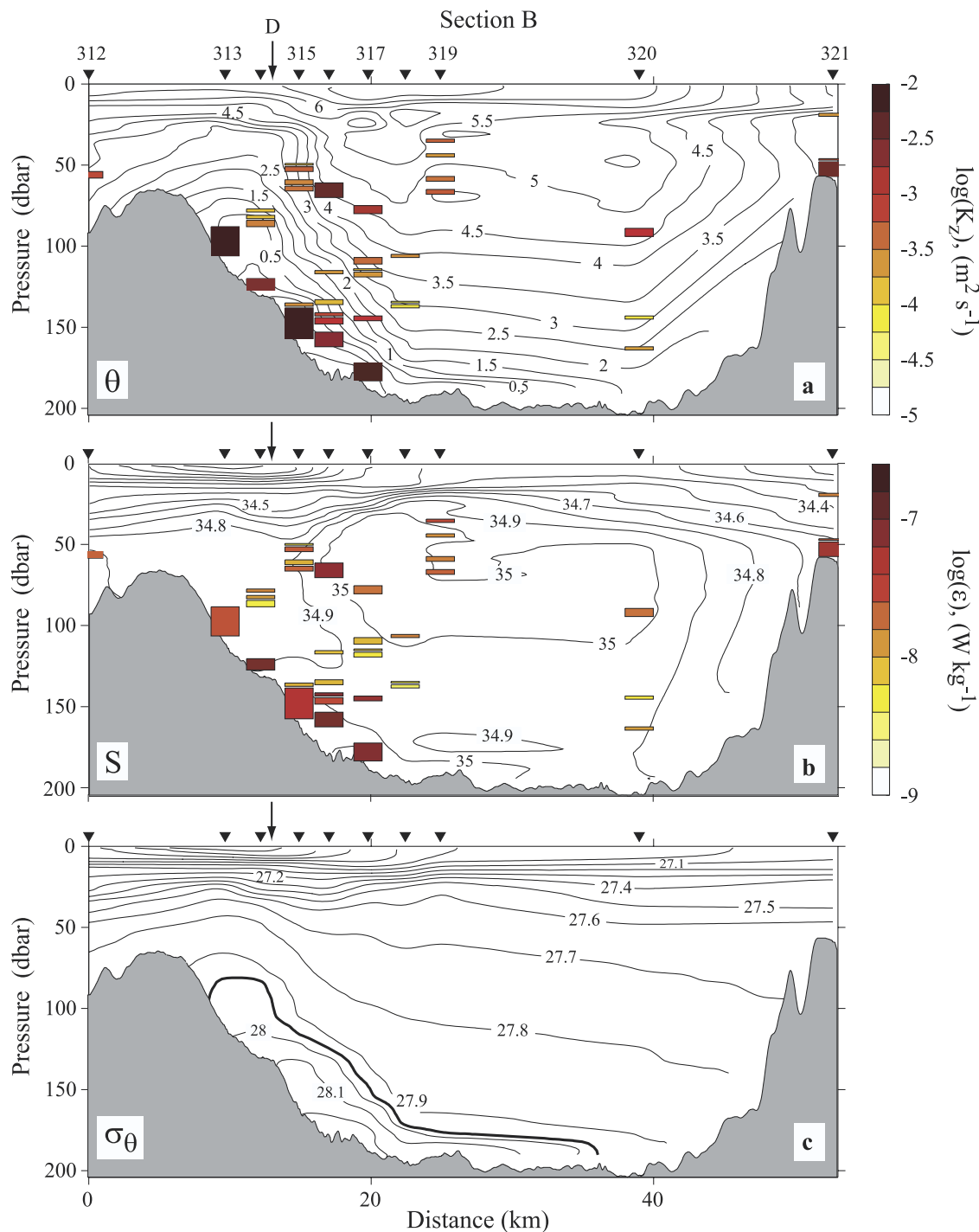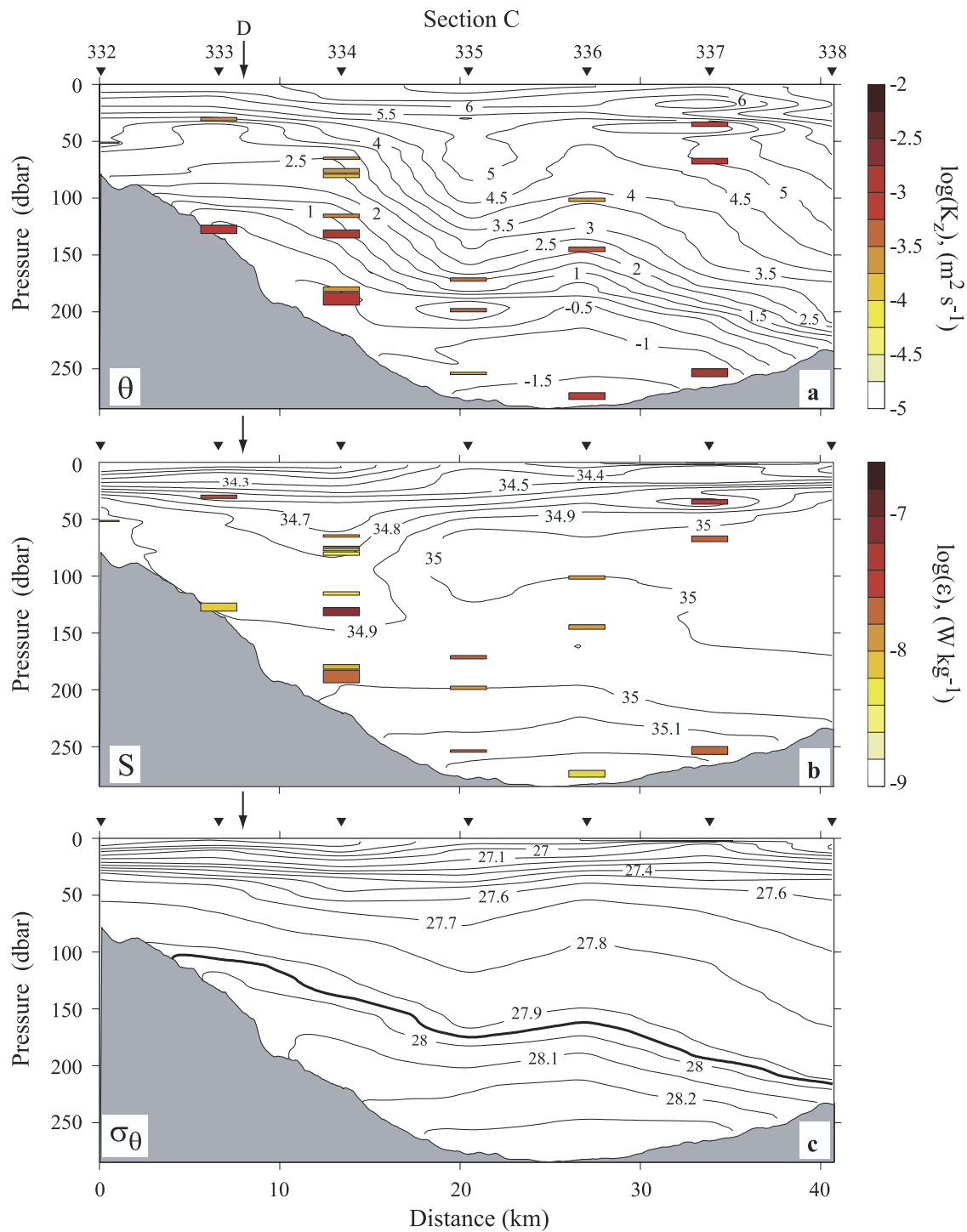
**Figure 8.** Same as Figure 7 but for section B. Note the enhanced mixing within the outflow where $\sigma_\theta > 27.9$.

tered prior to the survey since deep water with $\sigma_\theta > 28.3$ was not observed in section B.

### 4.2. Averaged Properties

[20] In order to get a survey-averaged picture, the estimates from 33 casts were sorted into 0.1 $\sigma_\theta$ unit bins and averaged. The average depth for each bin when $\sigma_\theta \leq 27.9$, i.e., from surface to slightly above the plume, and the average hab for $\sigma_\theta > 27.9$, comprising the plume, are calculated to obtain a density profile (Figure 10a). This approach was necessary to obtain a representative profile, which otherwise if depth-

averaged would have removed the signature of the overflow which descends from the sill depth of 120 m down to greater depths, adjacent to the bottom. Survey-averaged profiles of $\log(K_z)$ and $\log(\varepsilon)$ are calculated accordingly and shown in Figure 10 as a function of depth and hab. Here, errorbars show 95% confidence intervals of the mean over 200 bootstrap sampled populations. Dissipation rate typically decreases with depth from surface but increases substantially within the overflow. Vertical diffusivity remains fairly constant with depth until it increases by an order of magnitude within the plume. The heat flux is calculated using $Q =$

**Figure 9.** Same as Figure 7 but for section C.

$\rho C_p K_z d\theta/dz$, where $\rho$ is the density and $C_p$ is the specific heat of seawater, both calculated using the averaged temperature and salinity in each bin, $d\theta/dz$ is the average vertical temperature gradient. Values of heat flux obtained using $K_z$ suggest that the plume gains considerable amount of heat from the overlying AW. This can be compared to the rate of change of heat gain from section A to C. The change in section-averaged plume temperature between the two sections is $\Delta\theta = 0.5°C$. The heat gain, $\Delta H = \rho C_p \Delta\theta h$, is about $8 \times 10^7$ J m$^{-2}$ provided that the mean thickness of the plume h =

40 m. Assuming a constant speed of 10 cm s$^{-1}$, the plume will cover its path of x $\sim$ 80 km in $8 \times 10^5$ s which yields the rate of change of heat of about 100 W m$^{-2}$. This compares well, considering the uncertainty in $K_z$ (see section 3.2), with the values within the plume shown in Figure 10d.

### 4.3. Effects of Stratification

[21] The stratification modifies the dynamics of turbulence which is suppressed in strong stable stratification since more turbulent energy is needed to act against larger
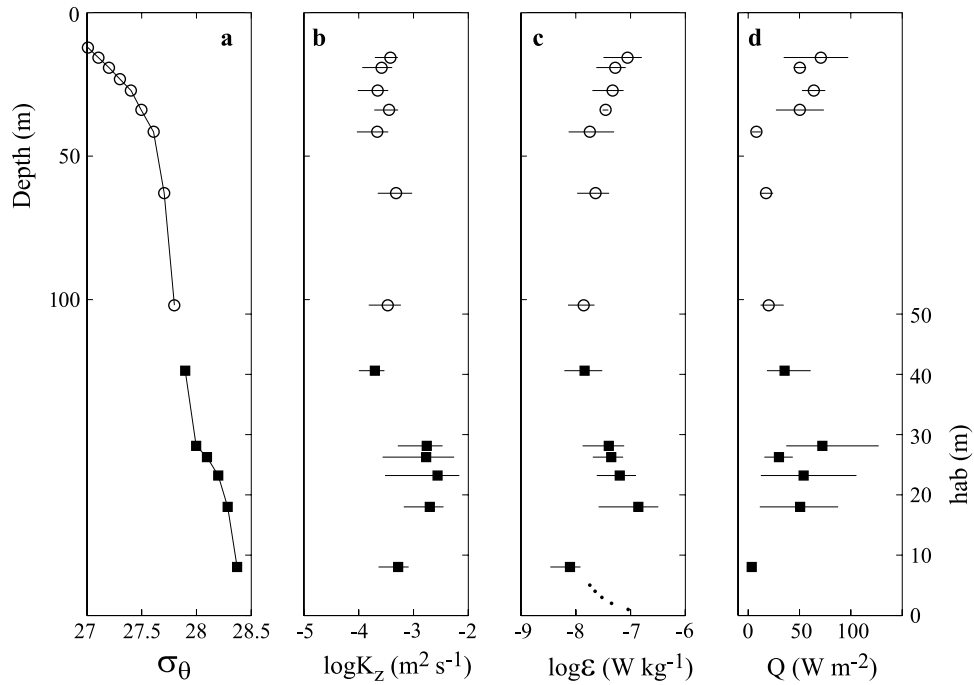
**Figure 10.** Survey-averaged profiles of $\sigma_\theta$, $K_z$, $\varepsilon$, and heat flux Q derived using 33 plume stations (dots in Figure 1), as a function of depth below surface (circles) until above the plume and hab (solid squares) within the plume. Averaged properties are calculated using 0.1 $\sigma_\theta$ unit bins, and error bars denote 95% bootstrap confidence intervals. Dots show the law of the wall estimates for $\varepsilon$ within 5 m to the bottom. Heat flux is positive when heat is transferred to deeper layers.
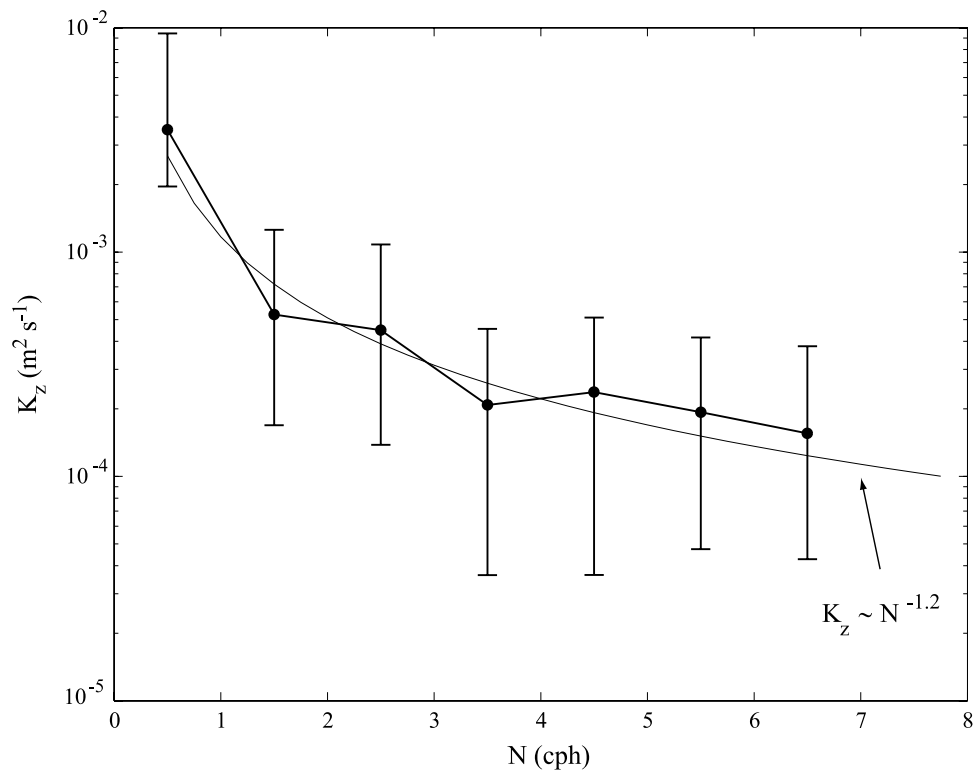


**Figure 11.** Variation of vertical diffusivity $K_z$ by buoyancy frequency N. Dots are the average values derived for each 1-cph bin, and error bars are 95% bootstrap confidence intervals. Best fit power law curve (thin line) shows $-1.2$ dependency.

vertical gradients of density. The ensemble of plume stations indicates a power law dependence of $K_z \sim N^{-1.2}$ (Figure 11). The 95% confidence interval for the exponent is ±0.3. This dependence is not conclusive since the variation in N is limited to less than one decade. Furthermore, time variability in small-scale shear can cause variability in $K_z$ which may appear related to N [*Rehmann and Duda*, 2000]. However, the decay of $K_z$ with increasing N is comparable to $\varepsilon \sim N^m$ with $1 \leq m \leq 2$, a range comprising that predicted for the midlatitude thermocline of the open ocean from six diverse sites [*Gregg*, 1989] and that obtained using observations of oceanic internal wave field in the literature [*Gargett and Holloway*, 1984]. This corresponds to $K_z \sim N^n$ with $-1 \leq n \leq 0$ using $K_z = \gamma\varepsilon/N^2$. However, using more extensive measurements with considerably more range in stratification and wave properties than has been previously available, *Polzin et al.* [1995] subsequently suggested $\varepsilon \sim N^2$ scaling as characteristic of the stratified interior of the deep sea. *D'Asaro and Lien* [2000] have recently offered an interpretation of two forms in terms of turbulence generated by different physics depending on the large-scale Richardson number (Ri = $N^2$/shear$^2$). They define a wave turbulence transition which separates two regimes: mixing controlled by interactions between internal wave modes (large Ri) and mixing controlled by instabilities of large-scale wave modes (Ri of order 1). For energies above this transition, $K_z \sim N^{-1}$ which is appropriate for diffusivities in lakes and fjords which are mixed by strong turbulent processes (e.g., mixing at the vicinity of a sill in fjords, rapid breakdown of intermittent seiches in lakes). For energies below the transition, diffusivity is independent of N (i.e., $\varepsilon \sim N^2$ consistent with the scaling of the stratified interior of the deep sea), and proportional to the squared internal wave spectral level. Our observations yield a scaling not significantly different than $K_z \sim N^{-1}$, and suggest that the mixing of the overflow is controlled by localized instability of large-scale motions, rather than transfer of energy from large-scale to smaller-scale turbulence due to wave-wave interactions. Inferring from scalar microstructure measurements, *Rehmann and Duda* [2000] examined the effect of stratification on $K_z$ for near-bottom mixing and for mixing throughout the water column. Near the bottom, they found a decay with N corresponding to n = −3.1, significantly larger than the values cited above. The discrepancy was attributed to different mechanisms driving the turbulence, as well as possible effects of entrainment. For mixing throughout the water column, they found n = −1.3 ± 0.8 comparable to our observations.

[22] Far from boundaries, turbulent fields are believed to be generated by random superposition of shear fields varying in time and space because of, for example, internal waves, leading to instabilities and turbulence provided that the field persists long enough to allow for a small-amplitude perturbation to grow. In case of a density current, if it is thin enough, i.e., comparable to the vertical length scale of turbulence, the mixing is determined by the turbulence generated near the boundary. Eddies will cover the entire dense layer leading to a homogeneous, mixed layer with small mixing across the interface [see *Turner*, 1973, section 4.3]. On the other hand, if the dense layer is thick, turbulent energy will decay away from the wall because of

viscous dissipation; hence wall effects on the interface will be negligible. The mixing at the interface is governed mainly by internal mixing mechanisms due to shear between the overflow and the ambient water, comparable to shear-induced mixing of internal waves in the thermocline. The Thorpe scale adjacent to the bottom is order of several meters (Figure 6b) and we might expect bottom-generated turbulence to decay within the overflow leading to the nearly homogeneous bottom layer (Figure 10a) consistent with the bottom layer defined by *Fer et al.* [2003, layer 1]. Enhanced mixing at the interface is due to internal mixing. When the velocity of inflow entrained into a turbulent gravity current is assumed proportional to the velocity of the current, with constant of proportionality equal to entrainment coefficient, E [*Ellison and Turner*, 1959], the buoyancy flux can be estimated by EuhN$^2$ [*Rehmann and Duda*, 2000]. Here, u is the mean speed relative to the ambient and h is the thickness of the dense layer. The buoyancy flux is also, by definition, equal to $K_z N^2$. Hence an estimate of E = $K_z$ (uh)$^{-1}$ can be derived. Using the mean value of $K_z$ within the overflow equal to $10 \times 10^{-4}$ m$^2$ s$^{-1}$ and u = 0.1 m s$^{-1}$, h = 40 m, we obtain E $\sim 3 \times 10^{-4}$, which compares well with the earlier estimates for the Storfjorden overflow [*Schauer and Fahrbach*, 1999; *Fer et al.*, 2003].

[23] Considerable work has been devoted to get reliable estimates of small-scale mixing through easily accessible and conventional methods. Direct measurements of turbulent shear, thus dissipation rate for homogeneous turbulence, or indirect estimates of turbulence parameters through scalar microstructure profiles, for example, via spectral methods, require large efforts to acquire highly specialized data. On the basis of temperature microstructure data covering 5 and 4 orders of magnitude in stratification and Thorpe scales, respectively, *Lorke and Wüest* [2002] provide strong evidence on universality of overturning-length-scale distributions, encouraging estimates of mixing from conventional, low-resolution profiles. In this study, observations by conventional profiling techniques highlight some of the mixing processes associated with the Storfjorden overflow. The vertical profiles allow distinctions to be made between mixing near the bottom, at the interface between the overflow and the ambient waters and off-slope waters at similar depths, using identical sampling and analysis techniques.

## References

Aagaard, K., L. K. Coachman, and E. Carmack (1981), On the halocline of the Arctic Ocean, *Deep Sea Res., Part A*, *28*, 529–545.

Anderson, L. G., E. P. Jones, R. Lindegren, B. Rudels, and P. I. Sehlstedt (1988), Nutrient regeneration in cold, high salinity bottom water of the Arctic shelves, *Cont. Shelf Res.*, *8*, 1345–1355.

Batchelor, G. K. (1953), *The Theory of Homogeneous Turbulence*, 197 pp., Cambridge Univ. Press, New York.

Cavalieri, D. J., and S. Martin (1994), The contribution of Alaskan, Siberian and Canadian coastal polynyas to the halocline layer of the Arctic Ocean, *J. Geophys. Res.*, *99*, 18,343–18,362.

D'Asaro, E. A., and R.-C. Lien (2000), The wave-turbulence transition for stratified flows, *J. Phys. Oceanogr.*, *30*, 1669–1678.

Dillon, T. M. (1982), Vertical overturns: A comparison of Thorpe and Ozmidov length scales, *J. Geophys. Res.*, *87*, 9601–9613.

Ellison, T. H., and J. S. Turner (1959), Turbulent entrainment in stratified flows, *J. Fluid Mech.*, *6*, 423–448.

Fer, I., R. Skogseth, P. M. Haugan, and P. Jaccard (2003), Observations of the Storfjorden overflow, *Deep Sea Res., Part I*, *50*, 1283–1303.

Ferron, B., H. Mercier, K. G. Speer, A. Gargett, and K. L. Polzin (1998), Mixing in the Romanche Fracture Zone, *J. Phys. Oceanogr.*, *28*, 1929–1945.

Galbraith, P. S., and D. E. Kelley (1996), Identifying overturns in CTD profiles, *J. Atmos. Oceanic Technol.*, *13*, 688–702.

Gargett, A. E., and G. Holloway (1984), Dissipation and diffusion by internal wave breaking, *J. Mar. Res.*, *42*, 15–27.

Gargett, A. E., T. R. Osborn, and P. W. Nasmyth (1984), Local isotropy and the decay of turbulence in a stratified fluid, *J. Fluid Mech.*, *144*, 231–280.

Gregg, M. C. (1987), Diapycnal mixing in the thermocline—A review, *J. Geophys. Res.*, *92*, 5249–5286.

Gregg, M. C. (1989), Scaling turbulent dissipation in the thermocline, *J. Geophys. Res.*, *94*, 9686–9698.

Griffiths, R. W. (1986), Gravity currents in rotating systems, *Annu. Rev. Fluid. Mech.*, *18*, 59–89.

Haarpaintner, J., P. M. Haugan, and J.-C. Gascard (2001), Interannual variability of the Storfjorden (Svalbard) ice cover and ice production observed by ERS-2 SAR, *Ann. Glaciol.*, *33*, 430–436.

Jungclaus, J. H., J. O. Backhaus, and H. Fohrmann (1995), Outflow of dense water from the Storfjord in Svalbard: A numerical model study, *J. Geophys. Res.*, *100*, 24,719–24,728.

Killworth, P. D. (1983), Deep convection in the world ocean, *Rev. Geophys.*, *21*, 1–26.

Lorke, A., and A. Wüest (2002), Probability density of displacement and overturning length scales under diverse stratification, *J. Geophys. Res.*, *107*(C12), 3214, doi:10.1029/2001JC001154.

Maus, S. (2002), Interannual variability of dense shelf water salinities in the Barents Sea, *Polar Res.*, *22*, 59–66.

Osborn, T. R. (1980), Estimates of the local rate of vertical diffusion from dissipation measurements, *J. Phys. Oceanogr.*, *10*, 83–89.

Ozmidov, R. V. (1965), On the turbulent exchange in a stably stratified ocean, *Atmos. Oceanic Phys.*, *8*, 853–860.

Pawlowicz, R., B. Beardsley, and S. Lenz (2002), Classical tidal harmonic analysis including error estimates in MATLAB using T-TIDE, *Comput. Geosci.*, *284*, 929–937.

Peltier, W. R., and C. P. Caulfield (2003), Mixing efficiency in stratified shear flows, *Annu. Rev. Fluid Mech.*, *35*, 135–167.

Polzin, K. L., J. M. Toole, and R. W. Schmitt (1995), Finescale parameterizations of turbulent dissipation, *J. Phys. Oceanogr.*, *25*, 306–328.

Price, J. F., and M. O. Baringer (1994), Outflows and deep water production by marginal seas, *Prog. Oceanogr.*, *33*, 161–200.

Quadfasel, D., B. Rudels, and K. Kurz (1988), Outflow of dense water from a Svalbard Fjord into the Fram Strait, *Deep Sea Res., Part A*, *35*, 1143–1150.

Rehmann, C. R., and T. F. Duda (2000), Diapycnal diffusivity inferred from scalar microstructure measurements near the New England Shelf/Slope front, *J. Phys. Oceanogr.*, *30*, 1354–1371.

Rudels, B., and D. Quadfasel (1991), Convection and deep water formation in the Arctic Ocean-Greenland Sea system, *J. Mar. Syst.*, *2*, 435–450.

Schauer, U. (1995), The release of brine-enriched shelf water from Storfjord into the Norwegian Sea, *J. Geophys. Res.*, *100*, 16,015–16,028.

Schauer, U., and E. Fahrbach (1999), A dense bottom water plume in the western Barents Sea: Downstream modification and interannual variability, *Deep Sea Res., Part I*, *46*, 2095–2108.

Schauer, U., B. Rudels, I. Fer, P. M. Haugan, R. Skogseth, G. Björk, and P. Winsor (2003), Return of deep shelf/slope convection in the western Barents Sea?, paper presented at the 7th Conference on Polar Meteorology and Oceanography and Joint Symposium on High-Latitude Climate Variations, Am. Meteorol. Soc., Hyannis, Mass.

Smethie, W. M., H. G. Ostlund, and H. H. Loosli (1986), Ventilation of the deep Greenland and Norwegian Seas: Evidence from Krypton-85, tritium, carbon-14, and argon-39, *Deep Sea Res., Part A*, *33*, 675–703.

Sternberg, R. W., K. Aagaard, D. Cacchione, R. A. Wheatcroft, R. A. Beach, A. T. Roach, and M. A. H. Marsden (2001), Long-term near-bed observations of velocity and hydrographic properties in the northeast Barents Sea with implications for sediment transport, *Cont. Shelf Res.*, *21*, 509–529.

Thorpe, S. A. (1977), Turbulence and mixing in a Scottish loch, *Philos. Trans. R. Soc. London, Ser. A*, *286*, 125–181.

Turner, J. S. (1973), *Buoyancy Effects in Fluids*, 367 pp., Cambridge Univ. Press, New York.

Wadhams, P. (2000), *Ice in the Ocean*, 351 pp., Gordon and Breach, Newark, N. J.

Yamazaki, H., and T. Osborn (1990), Dissipation estimates for stratified turbulence, *J. Geophys. Res.*, *95*, 9739–9744.

————————

I. Fer and P. M. Haugan, Geophysical Institute, University of Bergen, Allégaten 70, N-5007, Bergen, Norway. (ilker.fer@gfi.uib.no)

R. Skogseth, University Centre in Svalbard, P.O. Box 156, N-9171 Longyearbyen, Norway.